PAPER

Aluminum dendrite suppression by graphite coated anodes of Al-metal batteries†

Shiman He,‡[ab] Jie Wang,‡[a] Xu Zhang, [ID] *[a] Weiqin Chu,[a] Shu Zhao,[a] Daping He, [ID] [c] Min Zhu [ID] *[b] and Haijun Yu [ID] *[a]

Rechargeable aluminum batteries (RABs) are regarded as a promising energy storage system considering the high safety, rich abundance, and high capacity of aluminum. One of the critical challenges for RABs is the dendrite growth of Al, which arouses significant stability and safety issues. In this work, we demonstrate that a graphite coating layer can effectively protect the Al anode against dendrite growth. The Al metal batteries with graphite-coated Al anodes display lower overpotential (43 mV) and better cycling stability (400 h) than those with bare Al. Based on spike-like voltage profiles, metallic Al is found to be preferentially plated on the graphite layer rather than the Al substrate. In addition, the rough graphite coating layer with abundant interspace further regulates the plating/stripping behavior and accommodates the volume change of the Al anode. The dendrite growth of Al is significantly suppressed by graphite coating, which also favors high-performance RABs with a graphite cathode. This study sheds light on the facile and efficient suppression of Al dendrite growth toward RABs.

1. Introduction

Energy storage systems have become indispensable facilities in modern society, among which lithium-ion batteries (LIBs) are one of the most successful systems.[1] However, further applications of LIBs, especially grid-scale energy storage, are greatly limited by the low Li abundance and high cost.[2] Therefore, diverse secondary batteries relying on abundant resources have been developed.[3–6] Recently, rechargeable aluminum batteries (RABs) have become attractive because of the high capacity, low cost, and high safety of Al.[7] Specifically, the theoretical volumetric capacity of Al (8046 mA h cm^{-3}) is nearly four times higher than that of Li (2062 mA h cm^{-3}), making RABs a potential high-energy system.[8] Since the first room-temperature RAB was made by coupling a V_2O_5 cathode with an Al anode in an ionic liquid electrolyte in 2011,[9] plenty of cathode materials have been reported. In contrast, studies on Al anode materials, which are of universal merit for RABs as well as Al electrochemical metallurgy, are still insufficient.[10]

Dendrite growth has been considered one of the major issues that affects the electrochemical reversibility of RABs.[11–13] The dendrite growth of Al, which should be different from that of Li in mechanism, behavior, and electrochemical effect,[14–17] has been reported to destabilize the Al anode and reduce the plating/stripping efficiency of RABs.[10,18] However, until now, the comprehensive understanding and effective control of Al dendrite growth have been challenging. Al dendrites can cause uneven current distribution and inhomogeneous ion concentrations at the interface of Al electrodes, leading to reduced performance of RABs.[12,19] Moreover, nanosized aggregated Al dendrites would present less activity than pristine Al, which can significantly affect the voltage plateaus of RABs.[20,21] Some strategies have been proposed to suppress Al dendrite growth in RABs: (i) designing a porous Al structure by electrochemical etching to decrease the local current density;[10] (ii) coating the Al surface with Au particles exposed to the (111) plane to trigger epitaxial growth;[22] (iii) introducing liquid gallium (Ga) to enable reversible alloying/dealloying reactions between Al and Ga;[23,24] and (iv) adhering Al powder to form a porous structure and improve battery kinetic processes.[25] Despite the promising strategies proposed for suppressing dendrite growth in Al anodes, these methods are often complicated and expensive. Therefore, it is imperative to continue developing facile and cost-effective strategies to optimize Al anodes and improve the performance of RABs.

Herein, the graphite coating is demonstrated to be effective for suppressing the dendrite growth of Al toward high-

[a]Institute of Advanced Battery Materials and Devices, Key Laboratory of Advanced Functional Materials, Ministry of Education, Faculty of Materials and Manufacturing, Beijing University of Technology, Beijing, 100124, P. R. China. E-mail: hj-yu@bjut.edu.cn; zhangx@bjut.edu.cn

[b]Guangdong Provincial Key Laboratory of Advanced Energy Storage Materials, School of Materials Science and Engineering, South China University of Technology, Guangzhou, 510640, China. E-mail: memzhu@scut.edu.cn

[c]Hubei Engineering Research Center of RF-Microwave Technology and Application, Wuhan University of Technology, Wuhan, 430070, China

† Electronic supplementary information (ESI) available. See DOI: https://doi.org/10.1039/d3ta02404k

‡ The two authors contributed equally to this work.

performance RABs. Commercial Al foil with a graphite coating layer (Al-g) results in lower overpotential, better cycling stability, and higher coulombic efficiency (CE) when compared with bare Al foil, in either symmetric or asymmetric cells. Such an enhanced performance of the Al-g electrode can be ascribed to the suppressed dendrite growth of Al by a series of investigations. The controlling experiments and density functional theory (DFT) calculations suggest that metallic Al is preferentially plated on the graphite layer rather than the Al substrate. The graphite layer with ample interspace can accommodate volumetric change of metallic Al and promote uniform deposition. Therefore, the dendrite-free deposition of Al is realized, which prevents the cracks and irregular grains of Al and leads to extended electrochemical cycling and stable CE for RABs.

2. Results and discussion

The graphite coated Al electrode (Al-g), which is widely used as the current collector in LIBs, is applied to investigate the effect of graphite coating on the dendrite growth of Al. Two phases of Al-g are revealed by the X-ray diffraction (XRD, Fig. 1a) pattern, including graphite (PDF NO. 41-1487, black dot marked) and metallic Al (PDF NO. 04-0797, red rhombus marked).[26,27] The Raman spectrum of Al-g (Fig. 1b) shows a featured graphite profile with a weak defect-activated D peak ($\sim$1350 cm^{-1}), a strong G peak ($\sim$1580 cm^{-1}), and an I_D/I_G height ratio of $\sim$0.2, suggesting the relatively low defect density of the graphite coating layer.[28,29] Moreover, the scanning electron microscope (SEM) image (Fig. 1c) indicates that graphite nanosheets with an average size of $\sim$500 nm are stacked on the Al surface. The energy-dispersive X-ray spectroscopy (EDS) side-view elemental maps (Fig. 1d–f) demonstrate an enriched C distribution above the Al-rich region, in line with the graphite coating feature. The thickness of the graphite coating layer is estimated to be around 340 nm according to the EDS line scan (Fig. S1, ESI†).

To study the effect of the graphite coating layer on the electrochemical stability of the Al anode, symmetric cells with different electrodes were assembled using an electrolyte consisting of aluminum chloride/1-ethyl-3-methylimidazolium
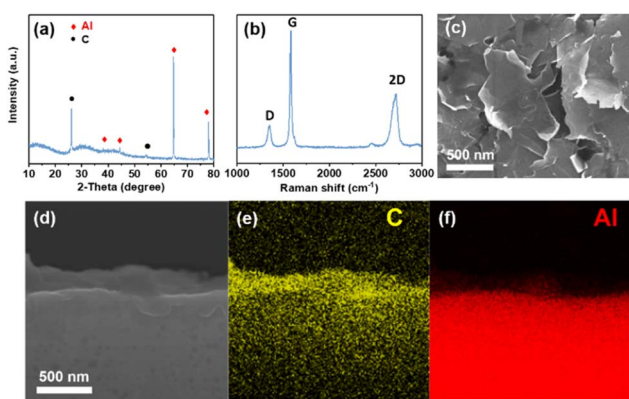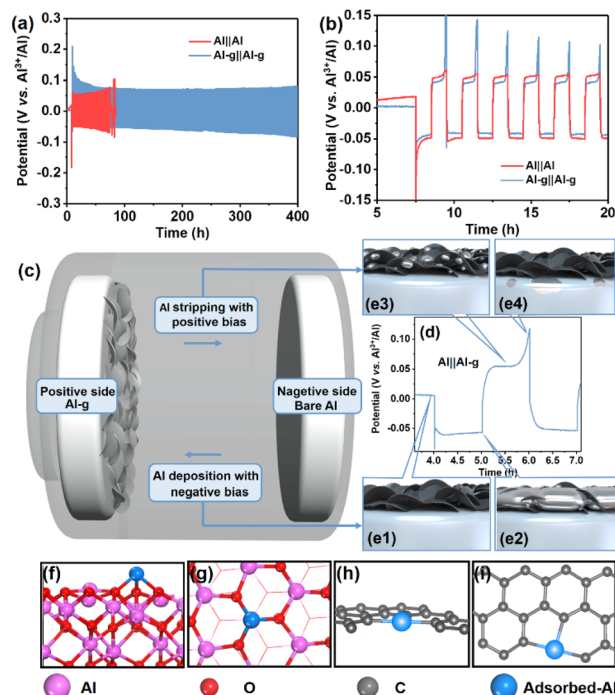

Fig. 2 (a) Electrochemical cycling of symmetric Al‖Al and Al-g‖Al-g cells. (b) Magnified profile of (a). (c and d) Configuration illustration of the asymmetrical Al‖Al-g cell (c) and the corresponding voltage–time profile (d). (e1–e4) Schematic diagrams of the Al stripping/plating processes on the Al-g electrode. (f–i) Geometrical configuration of Al atoms adsorbed on Al_2O_3 (f and g) and graphite (h and i).

chloride ($AlCl_3$/[EMIm]Cl, molar ratio 1.3/1). Fig. 2a displays the cycling stabilities of Al‖Al and Al-g‖Al-g symmetric cells, in which the current density and plating/stripping capacity are maintained at 0.4 mA cm^{-2} and 0.4 mA h cm^{-2}, respectively. It can be observed that the Al-g‖Al-g cell can stably cycle for more than 400 hours (blue line in Fig. 2a), while the Al‖Al cell suddenly short-circuits after 80 hours, suggesting superior stability of Al-g electrodes. At higher current densities of 0.8 and 1.2 mA cm^{-2}, the Al-g electrodes also exhibit better cycling performances over 250 and 80 hours, respectively (Fig. S2a and b†). Considering the graphite coating layer is the main difference between the Al‖Al and Al-g‖Al-g symmetric cells, the graphite coating layer can stabilize the Al-g electrode during plating/stripping processes.

The profile in the 0–40 h range in Fig. 2a was magnified in Fig. 2b to show more details. It is observed that the average polarization of the Al-g electrode (43 mV) is indeed smaller than that of the bare Al electrode (50 mV) if the spike-like voltage increase is ignored, which is only found at the end of the Al stripping process from the positive side (the end of the positive bias in each cycle). Similar situations were also found in the magnified profiles (Fig. S2c and d†) of symmetric cells with current densities of 0.8 and 1.2 mA cm^{-2}. When ignoring the spike-like voltage increase, the average polarizations of the Al-g electrode at 0.8 and 1.2 mA cm^{-2} were estimated to be 77 and 150 mV in the symmetric cells, respectively, both of which were smaller than those of bare Al electrodes (88 and 173 mV). This

Fig. 1 (a and b) XRD pattern (a) and Raman spectrum (b) of Al-g. (c) Top-view SEM image of Al-g. (d–f) Side-view SEM image (d) and the corresponding elemental distribution of C (e) and Al (f) of Al-g.

spike-like voltage increase is different from the case for the lithium metal anode occurring at the beginning of lithium plating due to the large polarization of lithium nucleation on the current collector.[30] Two cell configurations were examined to investigate the spike-like voltage increase: Al‖Al-g (Al: negative side and Al-g: positive side) and Al-g‖Al (Al-g: negative side and Al: positive side). The configurations of Al‖Al-g and Al-g‖Al cells are shown in Fig. 2c and S3a,† respectively. Interestingly, the spike-like voltage increase is not found in the voltage-time curve of the Al-g‖Al cell (Fig. S3b†), whereas it appears in the Al‖Al-g cell (Fig. 2c and d). This indicates that the increase in spike-like voltage only occurs when Al-g acts as a positive electrode with positive bias, corresponding to the Al stripping process from Al-g.

The Al‖Al-g cell was further examined by plating for 1 h and stripping for 2 h (excess stripping by 1 h) in the first cycle to evaluate the stripping behaviour of the Al-g electrode. As shown in the blue marked region in Fig. S4,† the fresh and active Al metal was plated on the graphite coating layer of the Al-g electrode in the first plating process. To further evidence the plating of Al on the graphite layer rather than beneath it, TEM investigation was employed. As shown in Fig. S5,† a graphite platelet scraped from the cycled Al-g electrode displays lattice fringes with an interplanar spacing of 0.205 nm, corresponding to the d-spacing of the (002) crystallographic planes of Al.[31] Combined with the elemental maps (Fig. S5b–S5f†), the structure of metallic Al plating on the graphite layer is clearly shown.

Subsequently, the Al-g electrode was stripped for 2 h, and the corresponding voltage curve can be divided into two regions: the orange marked region corresponding to the first 1 h and the green marked region corresponding to the second 1 h (Fig. S4†). During the first 1 h of stripping, the voltage curve also shows a relatively flat feature except for the spike-like voltage increase at the end, which corresponds to the dissolution of the newly plated Al on the graphite layer into the electrolyte. In contrast, during the second 1 h of stripping, the newly plated Al on the graphite layer being depleted led to the stripping reaction of the Al substrate beneath the graphite layer. Notably, the polarization of Al-g in the green marked region in Fig. S4† is consistently large throughout the whole stage. It is worth noting that the Al substrate beneath the graphite layer possesses a native alumina layer, thus resulting in a graphite–alumina–Al structure of the Al-g electrode.[32,33] Such a graphite–alumina–Al structure could be demonstrated by the electrochemical impedance spectrum (EIS, Fig. S6†), which displays one more semicircle than bare Al. It is reasonable that the overpotential of the newly plated active Al is lower than that of the Al substrate with a native alumina layer.[34–36] Therefore, the observed spike-like voltage increase at the end of the Al stripping process can be attributed to the rapid change in overpotential between the newly plated active Al and the Al substrate with a native alumina layer. And this phenomenon only occurs when the newly plated Al is depleted, corresponding to the end of the stripping process. This mechanism also explains the decay of the spike-like voltage increase in the following cycles, as the alumina layer underneath the graphite layer is gradually etched.

Based on the preceding discussion, the plating/stripping behaviour of the Al-g electrode is schematically illustrated in Fig. 2d and e. Fig. 2e1 depicts the initial state of the electrode, where the graphite layer is devoid of deposited Al metal. As a negative bias is applied to the symmetrical cell (Fig. 2e2), a substantial amount of Al metal gets deposited on the graphite layer. Subsequently, a significant proportion of the newly plated Al metal dissolves in the electrolyte from the graphite layer, forming a steady plateau at the positive bias (Fig. 2e3). Finally, the voltage sharply increases at the end of the stripping process due to the large impedance of the graphite–alumina–Al interface (Fig. 2e4). This plating/stripping behaviour of the Al-g electrode is proved by the SEM images (Fig. S7†) of the Al-g electrodes at different plating/stripping states. The plating/stripping behaviours of Al were further studied through theoretical calculations based on density functional theory (DFT). According to the above discussion, the alumina layer on the Al substrate beneath the graphite layer should not be ignored in the Al plating process.[32] Thus, we considered the presence of the alumina layer in the DFT calculations. The cross and top views of the geometrical configurations of alumina and adsorbed Al atoms are shown in Fig. 2f and g, respectively. The binding energy was calculated to probe the interactions between the absorbed Al atoms and the substrate. The molecular structures of adsorbed Al on the graphite layer are also exhibited in Fig. 2h and i. The calculation results show that graphite possesses lower binding energy (−1.77 eV) than alumina (−1.59 eV), suggesting that the Al nucleation tends to take place on the graphite matrix,[37,38] which is consistent with the experimental result that Al is preferentially plated on the graphite coating rather than the Al substrate.

Tafel plots were acquired to evaluate the kinetics of the Al-g electrode. The exchange current density can be obtained using
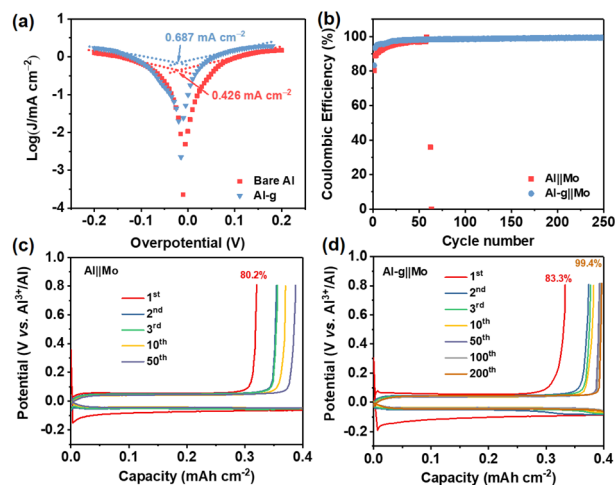

Fig. 3 (a) Tafel plots and the corresponding exchange current densities of bare Al and Al-g electrodes in asymmetric Al‖Mo and Al-g‖Mo cells, respectively. (b) CE comparison of Al deposition on Mo mesh at a current density of 0.4 mA cm⁻². The amount of Al plated in each cycle is 0.4 mA h cm⁻². (c and d) Voltage profiles of the Al plating/stripping process of cells with (c) Al anode and (d) Al-g anode at 0.4 mA cm⁻².

17022 | J. Mater. Chem. A, 2023, 11, 17020–17026

This journal is © The Royal Society of Chemistry 2023

the Tafel equation using the Tafel plots (Fig. 3a).[35] The Al-g electrode shows a higher exchange current density (0.687 mA cm^{-2}) than bare Al (0.426 mA cm^{-2}), indicating faster charge-transfer kinetics in the presence of a graphite layer. Moreover, asymmetric Al∥Mo and Al-g∥Mo cells were assembled to evaluate the coulombic efficiency (CE) of the plating/stripping behaviours of bare Al and Al-g anodes. Fig. 3b shows that the Al-g anode stably operates for 250 cycles with higher CEs, while the bare Al anode presents a quick decay of CEs after only 60 cycles. Significant differences can be observed in the corresponding voltage profiles (Fig. 3c and d) from CE measurements. Specifically, the Al-g∥Mo cell shows higher CE (83.3%) than the Al∥Mo cell (80.2%) in the first cycle. With an increase in the cycling number, less plated Al can be stripped back from the bare Al electrode, leading to a low CE of 35.9% in the 63rd cycle in the Al∥Mo cell (Fig. S8a†). In contrast, the CE of the Al-g∥Mo cell still remains at ∼99.4% after 200 cycles, which can be attributed to the graphite layer protecting Al and adjusting the plating/stripping processes. Additionally, Fig. S8b† shows that the Al∥Mo cell exhibits a voltage hysteresis of 83.7 mV in the 10th cycle, which increases to 112.6 mV in the 63rd cycle. In contrast, the Al-g∥Mo cell demonstrates a steady voltage hysteresis of only ∼72 mV even after 200 cycles. At higher current densities of 0.8 and 1.2 mA cm^{-2}, the asymmetric cells with Al-g anodes still stably show higher CEs and better cycling performances than bare Al anodes (Fig. S9 and S10†). These results indicate that the graphite coating layer greatly impacts the plating/stripping behaviours and improves the electrochemical reversibility of the Al anode. The electrochemical performances of state-of-the-art Al anodes are listed in Table S1.†[10,22,37,39–44] It is found that our Al-g anode shows competitive electrochemical performances. Considering the facile and low-cost features, the overall evaluation of this commercial Al-g electrode is attractive for the field of RABs.

Generally, the electrochemically deposited Al metal cannot maintain its original morphology during a prolonged deposition process due to the uneven current distribution on the electrode.[45,46] Thus, the morphology examination is necessary to gain information about the Al plating/striping process. Fig. 4a and S11a† show the SEM images of the electrode acquired from the symmetric cell with bare Al after 80 h. The images reveal the formation of numerous irregular aluminum grains on the surface. EDS mapping (Fig. S12a–c†) also demonstrates that the irregular morphology of the grains matches well with the Al elemental map. This rugged morphology is a representative feature of the plated Al dendrites, which will lead to the heterogeneous charge distribution and uneven deposition of Al (Fig. 4b). The subsequent plating/stripping processes of Al are also accompanied by further growth of Al grains, resulting in deeper cracks, severe volume changes, and internal pressure changes. In comparison, a flat morphology is observed in the SEM images (Fig. 4c and S11b†) of the cycled Al-g electrode, demonstrating a dense and uniform layer of Al metal with no noticeable Al dendrites after cycling. Fig. S12d–f† also display the homogeneous distribution of Al and C elemental maps on the cycled Al-g electrode. In addition, the XRD patterns and TEM image (Fig. S13†) of the cycled Al-g electrodes showed that the graphite coating layer still maintained its phase structure after long cycling.

Home-made *in situ* optical microscopy was carried out to further illustrate the growth process of Al deposition on bare Al and Al-g electrodes.[15] Both electrodes have smooth surfaces at the beginning of Al plating (Fig. 4e and f). Upon Al plating, protrusions start to appear along the edge of the planar Al metal within 10 min (Fig. 4e and Video S1, ESI†) and become more and more obvious after 30 min. The continuous growth of Al dendrites may cause internal short circuits, threatening the safety of batteries.[44] In contrast, the edge of the Al-g electrode remains smooth and free of Al dendrites (Fig. 4f and Video S2, ESI†) even after plating for 30 min. Such a growth behaviour is schematically displayed in Fig. 4d, which results in a uniform increase in thickness of the Al-g surface layer (red rectangle region in Fig. 4f). These results directly reveal that the coated graphite layer effectively stabilizes the interfaces and suppresses the dendrite growth of Al. As previously discussed, graphite possesses a lower binding energy than alumina when adsorbing the Al atom. Moreover, the rough features of the Al-g electrode can reduce the local current density, resulting in more uniform Al plating on the graphite coating layer and suppressing uneven dendrite growth of Al.[47] The presence of interspace in the graphite coating layer can accommodate the volume variation of Al during the plating/stripping processes and contribute to the stabilization of the Al anode. This effect is also found in carbon-based materials for lithium metal and zinc metal anodes.[48–50] As a result, the electrochemical performance of the graphite-coated Al anode is significantly improved, with a considerable reduction in Al dendrite growth.[39]

To further demonstrate the advantages of graphite-coated Al foil as the anode in RABs, Al and Al-g were coupled with a defect-free graphite film as cathode materials to assemble Al∥graphite and Al-g∥graphite dual-ion batteries using AlCl$_3$/EMIC electrolyte, respectively. The graphite cathode materials were prepared with a 2800 °C heating process, which has been proven to be an effective method to decrease the defect density.[28,51] A typical strong peak of the (002) plane of graphite was confirmed by the XRD pattern (Fig. S14a†). The Raman spectrum (Fig. S14b†) of the graphite cathode material shows no defect-activated D peak, revealing the high crystallinity and low defect density.[52] Such a graphite cathode material is promising to favor fine long-cycle and high-rate performance, which is suitable to evaluate the performance of Al anodes in RABs.[28] The charge/discharge profiles (Fig. 5a) of the Al∥graphite and Al-g∥graphite batteries show similar capacities, revealing that the graphite coating layer on the Al-g anode has little impact on the capacity. Notably, the discharged platform (∼1.7 V) of the Al-g∥graphite battery is slightly higher than that of the Al∥graphite battery. This observation is in agreement with the lower overpotential of the Al-g electrode in symmetric cells, which is also supported by the *CV* curves presented in Fig. 5b. Moreover, the *CV* curves reveal that the anodic peak located at around 2.3 V of the battery with the Al-g electrode is more negative than that with bare Al. The Al-g∥graphite battery also shows lower on-set potential of the charged plateau at around 2.3 V in Fig. 5a.
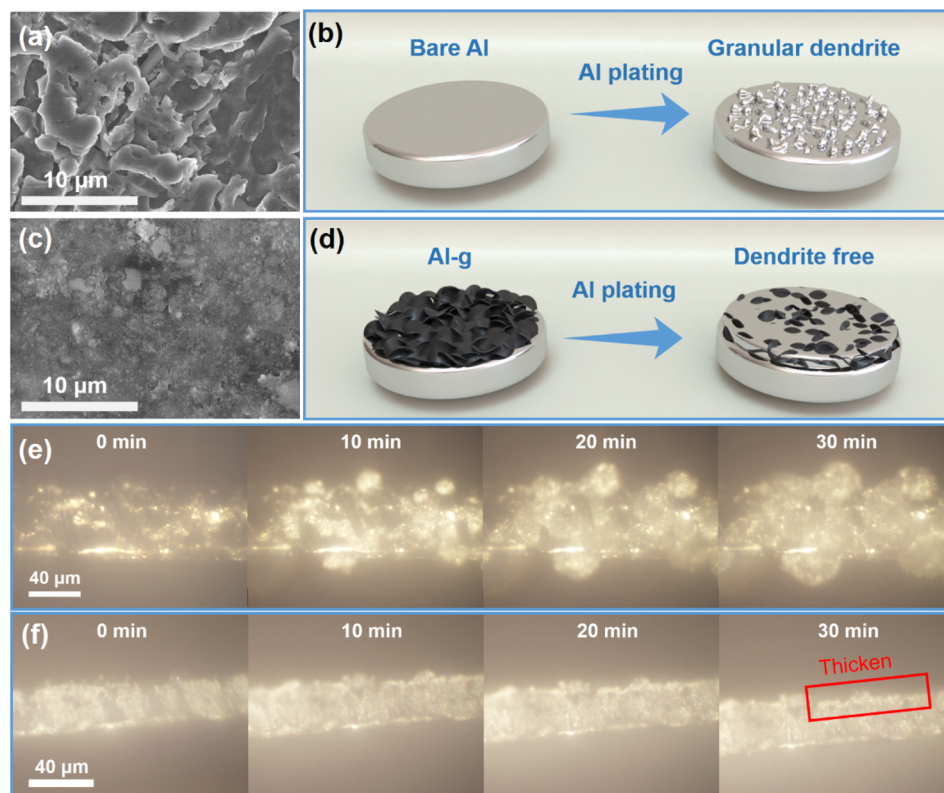
Fig. 4 (a–d) SEM images (a and c) and the corresponding Al deposition schematics (b and d) of cycled bare Al (a and b) and Al-g electrodes (c and d). (e and f) *In situ* optical microscopy images of Al (e) and Al-g (f) electrodes.
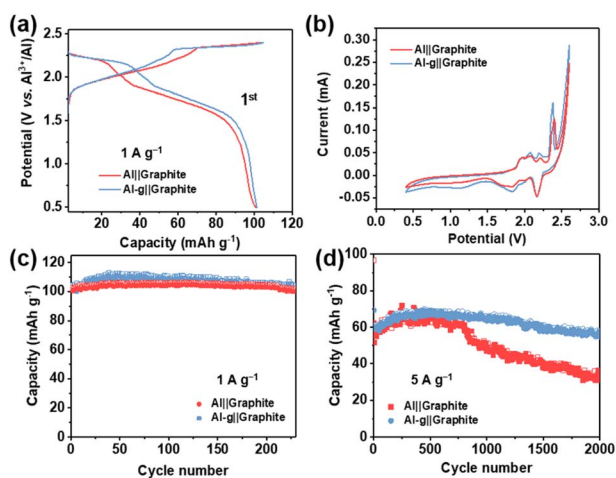

Fig. 5 (a) Galvanostatic discharge/charge curves and (b) *CV* curves of Al‖graphite and Al-g‖graphite batteries. (c and d) Cycling stability of Al‖graphite and Al-g‖graphite batteries at 1 A g^{-1} (c) and 5 A g^{-1} (d).

Moreover, Fig. 5c shows that the batteries with bare Al and Al-g anodes exhibit similar cycling stabilities at 1 A g^{-1}. This indicates that the Al dendrite growth in the bare Al anode is not significant enough to affect the cycling stability of the Al‖graphite batteries at low current density. The Al-g‖graphite battery (Fig. 5d) displays excellent cycling performance at 5 A g^{-1} with a capacity retention of 90% over 2000 cycles and high CE of

nearly 100%. In contrast, the Al‖graphite battery shows low capacity with rapid capacity decay within 700 cycles. The SEM images and corresponding EDS maps (Fig. S15 and S16†) of the cycled Al-g anode in the Al-g‖graphite battery demonstrate a smooth surface and homogeneous distribution of Al and C elements. And the rugged morphology of the cycled bare Al anode also verifies the growth of Al dendrites, which largely reduces the stability of the battery. The full-cell results further highlight the effective optimization of the Al anode by graphite coating owing to the adjustment of plating/stripping and suppression of dendrite growth of Al.

3. Conclusions

In conclusion, a graphite coating layer on the Al anode has demonstrated that it can greatly adjust the plating/stripping behaviors of Al and thereby suppress Al dendrite growth. The graphite coated Al (Al-g) shows much better cycle stability and lower overpotential than the bare Al anode. Based on a series of electrochemical investigations and DFT calculations, metallic Al is detected to be preferentially plated on a graphite layer. Moreover, the rough graphite structure on the Al-g surface can improve the current uniformity and provide space to tolerate the volume variations of Al. Therefore, the dendrite growth of Al is significantly suppressed, as evidenced by *ex situ* SEM and *in situ* optical microscopy. As a result, enhanced electrochemical stability can be realized in RABs with graphite as the cathode

17024 | *J. Mater. Chem. A*, 2023, **11**, 17020–17026

This journal is © The Royal Society of Chemistry 2023

material. These results provide important insight into the low-cost and compatible protection of the Al anode against dendrite growth toward high-performance RABs.

4. Experimental section

4.1. Materials

The Al foil (0.02 mm thick, 99.9%) was purchased from Beijing Trillion Metals Co., Ltd. Graphite coated Al (Al-g) was purchased from Kejing Materials Technology Co., Ltd. The ionic liquid electrolyte was prepared by slowly adding $AlCl_3$ (99%, Macklin Inc.) into 1-ethyl-3-methylimidazolium chloride ([EMIm]Cl, 98%, Aladdin Co., Ltd) in a molar ratio of 1.3 : 1 inside a Mikrouna argon glovebox. The graphite cathode material was prepared in the following steps. First, a graphene oxide (GO) suspension (Wuhan Hanene Technology Co., Ltd) with a concentration of 10–20 mg mL^{-1} was placed in a square dish and dried at room temperature for 24 h to form a GO film. Then, the GO film was annealed at 1300 °C for 2 h and then at 2800 °C for 1 h under Ar protection. Finally, the obtained graphite film was rolling compressed under 300 MPa to make it denser at 25–30 μm. Note that this graphite cathode material is not the graphite coating layer on the Al substrate.

4.2. Characterization

X-ray diffraction (XRD) was performed using a Bruker D8 Advance Diffractometer with Cu Kα radiation ($\lambda = 1.5406$ Å). Scanning electron microscopy (SEM) was carried out using a Hitachi S-4800 instrument. Raman spectra were acquired using a Renishaw analyzer ($\lambda_{laser} = 532$ nm). Transmission electron microscopy (TEM) images were obtained by using an FEI Themis Z instrument. *In situ* optical microscopy was used to investigate the Al deposition behavior. A quartz cell was used as the electrode housing, in which a symmetrical cell with bare Al or Al-g electrodes was assembled. The electrode area of the Al electrodes was 0.15 cm^2, and the distance between the two Al electrodes was ~0.5 cm. The electroplating/electrostripping current density was 1.0 mA cm^{-2}.

4.3. Computational method

All theoretical calculations were performed using density functional theory (DFT), as implemented in the Vienna *ab initio* simulation package (VASP).[53] The electron exchange and correlation energy were treated within the generalized gradient approximation in the Perdew–Burke–Ernzerhof functional (GGA-PBE).[54] The plane-wave cut-off is 400 eV. Spin polarization was considered in all the computations. The convergence criteria for the electronic self-consistent iteration and force were set to 10^{-5} eV and 0.02 eV Å^{-1}, respectively.

4.4. Electrochemical measurements

Al‖Al symmetric cells and Al‖Mo half cells with both pieces of Al and Al-g foil were assembled inside the Ar glovebox with the $AlCl_3$/[EMIm]Cl electrolyte in Swagelok-type configuration. Al‖graphite dual-ion batteries were assembled using the as-prepared graphite as the cathode, Whatman Glass fiber as the

separator, and Al or Al-g foil as the anode in Swagelok-type configuration. The mass loading of the active material is about 3–4 mg cm^{-2}, and the mass of the electrolyte is about 50 mg. The electrochemical performance of these batteries was tested using a Land instrument (Wuhan LAND Electronics Co., Ltd) at 25 °C. A cyclic voltammogram (CV) was recorded on a Solartron electrochemical workstation. The electrochemical impedance spectroscopy (EIS) test was performed on a CHI electrochemical workstation with an AC voltage of 5 mV amplitude in the frequency range from 100 kHz to 0.01 Hz.

Conflicts of interest

There are no conflicts to declare.

Acknowledgements

References

1 R. Khurana, J. L. Schaefer, L. A. Archer and G. W. Coates, *J. Am. Chem. Soc.*, 2014, **136**, 7395–7402.

2 S. He, D. Zhang, X. Zhang, S. Liu, W. Chu and H. Yu, *Adv. Energy Mater.*, 2021, **11**, 2100769.

3 Y. You, S. Xin, H. Y. Asl, W. Li, P.-F. Wang, Y.-G. Guo and A. Manthiram, *Chem*, 2018, **4**, 2124–2139.

4 Z. Liu, P. Li, G. Suo, S. Gong, W. Wang, C.-Y. Lao, Y. Xie, H. Guo, Q. Yu, W. Zhao, K. Han, Q. Wang, M. Qin, K. Xi and X. Qu, *Energy Environ. Sci.*, 2018, **11**, 3033–3042.

5 L. L. Chen, W. L. Song, N. Li, H. Jiao, X. Han, Y. Luo, M. Wang, H. Chen, S. Jiao and D. Fang, *Adv. Mater.*, 2020, **32**, 2001212.

6 H. Li, C. Han, Y. Huang, Y. Huang, M. Zhu, Z. Pei, Q. Xue, Z. Wang, Z. Liu, Z. Tang, Y. Wang, F. Kang, B. Li and C. Zhi, *Energy Environ. Sci.*, 2018, **11**, 941–951.

7 D. J. Kim, D.-J. Yoo, M. T. Otley, A. Prokofjevs, C. Pezzato, M. Owczarek, S. J. Lee, J. W. Choi and J. F. Stoddart, *Nat. Energy*, 2019, **4**, 51–59.

8 S. He, J. Wang, X. Zhang, J. Chen, Z. Wang, T. Yang, Z. Liu, Y. Liang, B. Wang, S. Liu, L. Zhang, J. Huang, J. Huang, L. A. O'Dell and H. Yu, *Adv. Funct. Mater.*, 2019, **29**, 1905228.

9 N. Jayaprakash, S. K. Das and L. A. Archer, *Chem. Commun.*, 2011, **47**, 12610–12612.

10 Y. Long, H. Li, M. Ye, Z. Chen, Z. Wang, Y. Tao, Z. Weng, S. Qiao and Q.-H. Yang, *Energy Storage Mater.*, 2021, **34**, 194–202.

11 F. Wu, N. Zhu, Y. Bai, Y. Gao and C. Wu, *Green Energy Environ.*, 2018, **3**, 71–77.

This journal is © The Royal Society of Chemistry 2023

J. Mater. Chem. A, 2023, **11**, 17020–17026 | **17025**

12 D.-M. She, W.-L. Song, J. He, N. Li, H. Chen, S. Jiao and D. Fang, *J. Electrochem. Soc.*, 2020, **167**, 130530.

13 H. Chen, H. Xu, B. Zheng, S. Wang, T. Huang, F. Guo, W. Gao and C. Gao, *ACS Appl. Mater. Interfaces*, 2017, **9**, 22628–22634.

14 K. Liu, A. Pei, H. R. Lee, B. Kong, N. Liu, D. Lin, Y. Liu, C. Liu, P. C. Hsu, Z. Bao and Y. Cui, *J. Am. Chem. Soc.*, 2017, **139**, 4815–4820.

15 X.-B. Cheng, C. Yan, X. Chen, C. Guan, J.-Q. Huang, H.-J. Peng, R. Zhang, S.-T. Yang and Q. Zhang, *Chem*, 2017, **2**, 258–270.

16 J. Zheng, M. H. Engelhard, D. Mei, S. Jiao, B. J. Polzin, J.-G. Zhang and W. Xu, *Nat. Energy*, 2017, **2**, 17012.

17 Y. Liu, X. Tao, Y. Wang, C. Jiang, C. Ma, O. Sheng, G. Lu and X. W. Lou, *Science*, 2022, **375**, 739–745.

18 M. Jiang, C. Fu, P. Meng, J. Ren, J. Wang, J. Bu, A. Dong, J. Zhang, W. Xiao and B. Sun, *Adv. Mater.*, 2022, **34**, 2102026.

19 B. Craig, T. Schoetz, A. Cruden and C. Ponce de Leon, *Renewable Sustainable Energy Rev.*, 2020, **133**, 110100.

20 D. Muñoz-Torrero, P. Leung, E. García-Quismondo, E. Ventosa, M. Anderson, J. Palma and R. Marcilla, *J. Power Sources*, 2018, **374**, 77–83.

21 L. D. Reed and E. Menke, *J. Electrochem. Soc.*, 2013, **160**, A915–A917.

22 Q. Zhao, J. Zheng, Y. Deng and L. Archer, *J. Mater. Chem. A*, 2020, **8**, 23231–23238.

23 H. Jiao, S. Jiao, S. Li, W.-L. Song, H. Chen, J. Tu, M. Wang, D. Tian and D. Fang, *Chem. Eng. J.*, 2020, **391**, 123594.

24 X. Shen, T. Sun, L. Yang, A. Krasnoslobodtsev, R. Sabirianov, M. Sealy, W. N. Mei, Z. Wu and L. Tan, *Nat. Commun.*, 2021, **12**, 820.

25 N. Li, D. She, K. Zhang, H.-S. Chen, W.-L. Song and S. Jiao, *Chemsuschem*, 2022, **15**, e202201390.

26 X. Dong, H. Xu, H. Chen, L. Wang, J. Wang, W. Fang, C. Chen, M. Salman, Z. Xu and C. Gao, *Carbon*, 2019, **148**, 134–140.

27 D. Lee, G. Lee and Y. Tak, *Nanotechnology*, 2018, **29**, 36LT01.

28 H. Chen, F. Guo, Y. Liu, T. Huang, B. Zheng, N. Ananth, Z. Xu, W. Gao and C. Gao, *Adv. Mater.*, 2017, **29**, 1605958.

29 J. Wang, X. Zhang, W. Chu, S. Liu and H. Yu, *Chem. Commun.*, 2019, **55**, 2138–2141.

30 G. Zheng, S. W. Lee, Z. Liang, H. W. Lee, K. Yan, H. Yao, H. Wang, W. Li, S. Chu and Y. Cui, *Nat. Nanotechnol.*, 2014, **9**, 618–623.

31 Y. Li, W. Song, C. Xie, D. Zeng, A. Wang and M. Hu, *Mater. Chem. Phys.*, 2006, **97**, 127–131.

32 J. D. Baran, H. Gronbeck and A. Hellman, *Phys. Rev. Lett.*, 2014, **112**, 146103.

33 P. Cornette, D. Costa and P. Marcus, *J. Electrochem. Soc.*, 2020, **167**, 161501.

34 S. Choi, H. Go, G. Lee and Y. Tak, *Phys. Chem. Chem. Phys.*, 2017, **19**, 8653–8656.

35 F. J. Martin, G. T. Cheek, W. E. O'Grady and P. M. Natishan, *Corros. Sci.*, 2005, **47**, 3187–3201.

36 H. Wang, S. Gu, Y. Bai, S. Chen, F. Wu and C. Wu, *ACS Appl. Mater. Interfaces*, 2016, **8**, 27444–27448.

37 Y. Meng, M. Wang, K. Li, Z. Zhu, Z. Liu, T. Jiang, X. Zheng, K. Zhang, W. Wang, Q. Peng, Z. Xie, Y. Wang and W. Chen, *Nano Lett.*, 2023, **23**, 2295–2303.

38 Y. Fang, S. L. Zhang, Z.-P. Wu, D. Luan and X. W. Lou, *Sci. Adv.*, 2021, **7**, eabg3626.

39 J. Li, K. S. Hui, S. Ji, C. Zha, C. Yuan, S. Wu, F. Bin, X. Fan, F. Chen, Z. Shao and K. N. Hui, *Carbon Energy*, 2022, **4**, 155–169.

40 Z. Zhang, X. Yang, P. Li, Y. Wang, X. Zhao, J. Safaei, H. Tian, D. Zhou, B. Li, F. Kang and G. Wang, *Adv. Mater.*, 2022, **34**, e2206970.

41 N. Lindahl, J. Bitenc, R. Dominko and P. Johansson, *Adv. Funct. Mater.*, 2020, **30**, 2004573.

42 S. Ha, J. C. Hyun, J. H. Kwak, H.-D. Lim, B. S. Youn, S. Cho, H.-J. Jin, H.-K. Lim, S. M. Lee and Y. S. Yun, *Chem. Eng. J.*, 2022, **437**, 135416.

43 J. Yoon, S. Moon, S. Ha, H.-K. Lim, H.-J. Jin and Y. S. Yun, *J. Energy Chem.*, 2022, **74**, 121–127.

44 H. Jiao, S. Jiao, W.-L. Song, X. Xiao, D. She, N. Li, H. Chen, J. Tu, M. Wang and D. Fang, *Nano Res.*, 2021, **14**, 646–653.

45 X. B. Cheng, R. Zhang, C. Z. Zhao and Q. Zhang, *Chem. Rev.*, 2017, **117**, 10403–10473.

46 Z. Liang, G. Zheng, C. Liu, N. Liu, W. Li, K. Yan, H. Yao, P. C. Hsu, S. Chu and Y. Cui, *Nano Lett.*, 2015, **15**, 2910–2916.

47 J. Zheng, D. C. Bock, T. Tang, Q. Zhao, J. Yin, K. R. Tallman, G. Wheeler, X. Liu, Y. Deng, S. Jin, A. C. Marschilok, E. S. Takeuchi, K. J. Takeuchi and L. A. Archer, *Nat. Energy*, 2021, **6**, 398–406.

48 D. J. Kautz, L. Tao, L. Mu, D. Nordlund, X. Feng, Z. Zheng and F. Lin, *J. Mater. Chem. A*, 2018, **6**, 16003–16011.

49 Q. Zhao, X. Hao, S. Su, J. Ma, Y. Hu, Y. Liu, F. Kang and Y.-B. He, *J. Mater. Chem. A*, 2019, **7**, 15871–15879.

50 Y. Zeng, P. X. Sun, Z. Pei, Q. Jin, X. Zhang, L. Yu and X. W. D. Lou, *Adv. Mater.*, 2022, **34**, e2200342.

51 C. Fan, B. Wu, R. Song, Y. Zhao, Y. Zhang and D. He, *Carbon*, 2019, **155**, 506–513.

52 H. Chen, C. Chen, Y. Liu, X. Zhao, N. Ananth, B. Zheng, L. Peng, T. Huang, W. Gao and C. Gao, *Adv. Energy Mater.*, 2017, **7**, 1700051.

53 G. Kresse and J. Furthmüller, *Comput. Mater. Sci.*, 1996, **6**, 15–50.

54 J. P. Perdew, K. Burke and M. Ernzerhof, *Phys. Rev. Lett.*, 1996, **77**, 3865–3868.

17026 | *J. Mater. Chem. A*, 2023, **11**, 17020–17026

This journal is © The Royal Society of Chemistry 2023